International Journal of Scientific Research in Computer Science and Engineering
Vol.10, Issue.2, pp.16-29, April (2022)

Research Paper

E-ISSN: 2320-7639

Dynamic Analysis of Synchronous Machine at Varied Excitation Voltage and Quadrature axis Reactance

Crescent Onyebuchi Omeje[1*], Stephen Ejiofor Oti[2]

[1]Department of Electrical/Electronic Engineering, University of Port Harcourt, Rivers State Nigeria
[2]Department of Electrical Engineering, University of Nigeria, Nsukka Enugu State Nigeria

**Corresponding Author: crescent.omeje@uniport.edu.ng, Tel: +2348032645484*

Available online at: www.isroset.org

Received: 21/Jan/2022, Accepted: 28/Mar/2022, Online: 30/Apr/2022

Abstract — The effects of a varied d.c excitation voltage on the speed and power output of two selected synchronous machines were analyzed in this paper through computer simulations. The steady state equations for a cylindrical rotor and salient pole synchronous machines were derived and simulated at different values of quadrature axis reactance. A varied excitation voltage values were also considered while a significant increase in the value of power output for the salient pole machine was obtained after simulation. The cylindrical rotor machine remained unaffected by the variation in the quadrature axis reactance. The dynamic equations for a salient pole machine were also modeled and simulated with simplified algorithms using embedded MATLAB Function block in ideal motor operating condition and under a three phase to ground fault. The simulation results showed an increase in real power and reactive power values at an increased excitation voltage. A rapid drop in speed and torque value was observed during a three phase to ground fault and was restored after six seconds. All Simulation results were achieved in MATLAB/Simulink software.

Keywords— DC-Excitation; Dynamic Modeling; Real Power; Reactive Power; Synchronous Machine, Speed and Torque control.

1. INTRODUCTION

Synchronous machines are a.c machines that compete favourably with the induction machine in many industrial applications. They are generally more expensive and more complex in terms of variable speed control than the induction machine drives [1, 2]. Synchronous machines are mostly used in hydro and thermal power station for electricity generation. The speed of the machine under steady state condition is always proportional to the frequency of the rotating magnetic flux in the armature and it runs at a synchronous speed value equivalent to its rated speed value [3]. The magnetic field produced by the armature currents rotates at the same speed with the field current produced on the rotor which rotates at the synchronous speed value [3]. The synchronous machine unlike the induction machine operates in lagging power factor mode when under excited, in unity power factor mode when normally excited and in leading power factor mode when overexcited by simply adjusting the machine rated current [4]. The synchronous machine requires a simultaneous supply of a.c voltage to the stator windings and d.c excitation voltage or field current on the rotor field windings and therefore is not self-starting [5]. The rotor of the machine is turned into rotation by a prime mover which produces a rotating magnetic field within the machine. The d.c current applied to the rotor is achieved from an external d.c source connected to the rotor through slip rings and brushes. This process can also be realized through a specialized d.c power source mounted directly on the shaft of the machine usually a rotating rectifier which is commonly referred to as a brushless d.c machine [5].

II. RELATED WORK

Many research works have been conducted and presented on synchronous machine modeling and analysis. In [6], the d-q model of synchronous machine was carried out for sensor-less control operation while a small signal finite element modeling of synchronous machine was presented in [7]. A small signal modeling for virtual synchronous generator was detailed in [8]. The comparison of different synchronous machines for sensor-less drives was analyzed in [9,10]. Optimal design of wound field synchronous reluctance machine that improves torque through the increase in the saliency ratio was presented in [11]. The above research papers exhaustively discussed the dynamic characteristics of the synchronous machine with emphasis on small signal injection, an increased saliency ratio and sensor-less drives. This paper in a different view focused on the effects of varied field excitation and quadrature axis reactance on the power output of the synchronous machines which were achieved through computer simulations. The machines steady state and dynamic equations were modeled and presented with their respective phasor and circuit diagrams for clarity. A simplified algorithm for the speed control was adopted for the satisfactory simulation of the salient pole machine dynamics in its ideal state and under a three phase to ground fault. An aberration in the speed and torque

oscillation was observed under a three phase to ground fault as presented in the preceding simulation results.

A synchronous machine attains a steady state condition if the entire transient disturbance such as a sudden change in load and transitory oscillations are attenuated with a constant speed and torque sustained [12]. A three phase current flows in the stator winding of a synchronous machine when connected to an a.c voltage supply of fixed frequency (busbar). This creates a rotating magnetic field which rotates at a synchronous speed value. The rotor (field winding) at this point is usually stationary and hardly picks up speed instantaneously due to inertia. The magnetic rotatory field and the rotor field winding move relative to each other resulting in zero average torque. A d.c exciter is usually placed across the rotor field winding which produces a magnetic field that rotates at a synchronous speed value. The field interaction between the stator and rotor which rotates at synchronous speed produces a steady state constant torque. The steady state analysis presented in this paper considered the cylindrical (round) rotor and salient pole synchronous machine in relation to their mechanical output power and torque for varying excitation. The cylindrical rotor synchronous machine is usually suited for high speed operation such as steam turbine and turbo generator applications due to a reduced number of poles and circumferential diameter of uniform air-gap. Its structural representation is presented in Figure 1. The salient pole machine contrariwise has a large diameter with more number of poles and is designed for low speed operation with specific application in hydroelectric power generation. Traditional applications for the salient pole motor are pump systems, paper mills, ship propulsion and other applications with moderate dynamic requirements [13]. Its diagram is presented in Figure 2.

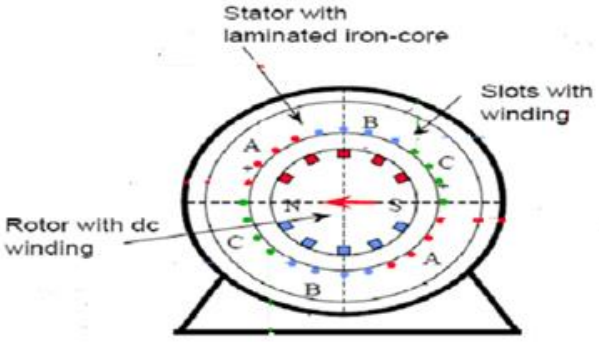

Figure 1: Cylindrical Rotor Synchronous machine

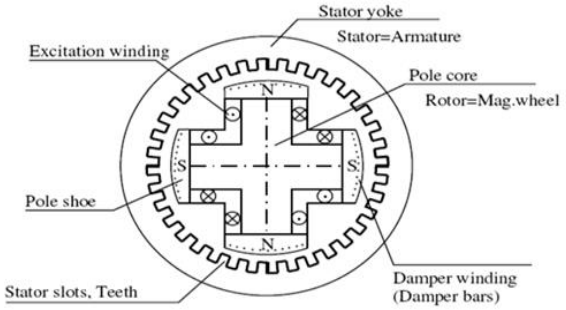

Figure 2: Salient Pole Synchronous machine.

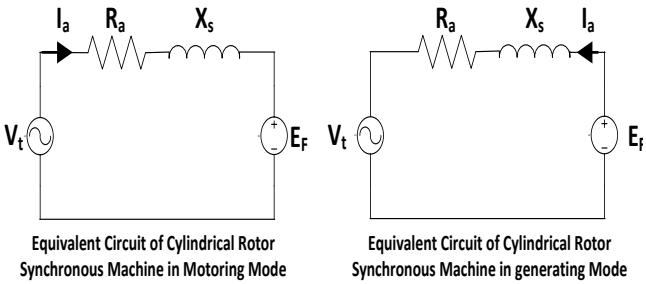

Figure 3: Equivalent circuit diagrams of cylindrical rotor synchronous machine in motoring and generating modes.

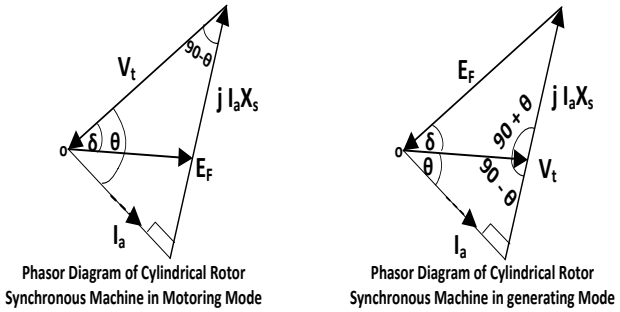

Figure 4: Equivalent phasor diagrams of cylindrical rotor synchronous machine in motoring and generating modes.

The equivalent circuits of the cylindrical rotor machine are presented in Figure 3 with the corresponding phasor diagrams shown in Figure 4. The voltage equations of a cylindrical rotor synchronous machine as derived from the phasor diagram in Figure 4 are presented in equations (1) and (2) for motoring and generating modes.

$$V_t = E_F + I_a (R_a + jX_s) \quad (1)$$

$$V_t = E_F - I_a (R_a + jX_s) \quad (2)$$

The power developed with armature resistance and rotational losses neglected is given by equation (3)

$$P_{output} = P_e = \frac{3E_F V_t \sin\delta}{X_s} \quad (3)$$

The voltage equations for the salient pole synchronous machine under generating mode is derived from Figure 5 and presented in equations (4) and (5). In motoring mode, the voltage equations are derived from Figure 6 and presented in equations (6), (7) and (8) respectively.

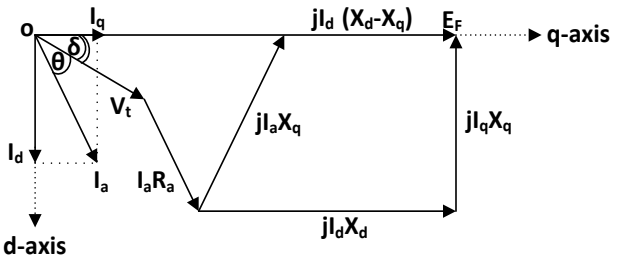

Figure 5: Equivalent phasor diagram of salient pole synchronous machine in generating mode.

$$E_F = V_t + I_a R_a + jX_d I_d + jX_q I_q \quad (4)$$

$$E_F = V_t + I_aR_a + jI_aX_q + j\,I_d\,(X_d - X_q) \quad (5)$$

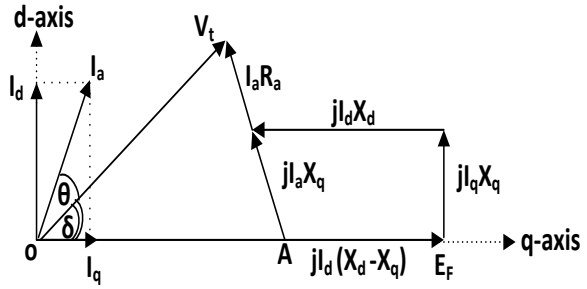

Figure 6: Equivalent phasor diagram of salient pole synchronous machine in motoring mode.

$$E_F = OA + jI_d(X_d - X_q) \quad (6)$$
$$V_t = OA + I_aR_a + jI_aX_q \quad (7)$$
$$OA = V_t - I_a(R_a + jX_q) \quad (8)$$

Substituting (8) into (6) gives rise to (9).

$$E_F = V_t - I_a(R_a + jX_q) + jI_d(X_d - X_q) \quad (9)$$

Re-arranging (9) with V_t made subject of the formula gives rise to (10)

$$V_t = E_F + I_a(R_a + jX_q) - jI_d(X_d - X_q) \quad (10)$$

On infinite bus bars, the armature resistance becomes very negligible. The phasor diagram in Figure 5 is modified with zero armature resistance and represented in Figure 7.

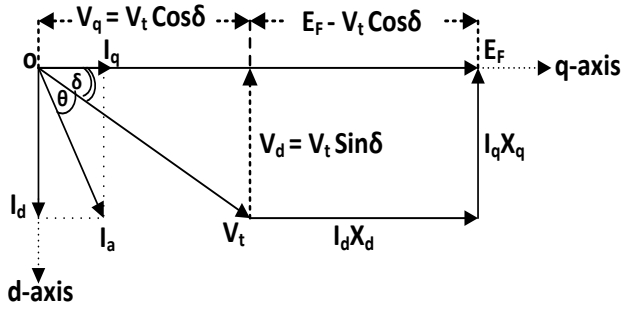

Figure 7: Equivalent phasor diagram of salient pole synchronous generator on infinite bus bar.

The net electrical power output P_o is the sum of the products of the d-q phase components of the respective voltage and current as presented in equation (11) for a three phase connected machine.

$$P_0 = 3(V_dI_d + V_qI_q) \quad (11)$$

The d-q axis voltage and current equations are derived from Figure 7 and represented in equations (12) – (15).

$$V_d = V_t \sin\delta \quad (12)$$
$$V_q = V_t \cos\delta \quad (13)$$
$$I_d = \frac{E_F - V_t \cos\delta}{X_d} \quad (14)$$
$$I_q = \frac{V_t \sin\delta}{X_q} \quad (15)$$

Substituting equations (12) to (15) into equation (11) gives rise to equation (16).

$$P_0 = 3\left(\frac{V_t \sin\delta}{X_d}(E_F - V_t \cos\delta) + \frac{V_t \cos\delta}{X_q}(V_t \sin\delta)\right) \quad (16)$$

Re-arranging equation (16) gives rise to equation (17) which represents the steady state output power of a salient pole synchronous machine.

$$P_0 = 3\left(\frac{V_t E_F \sin\delta}{X_d} + \frac{V_t^2(X_d - X_q)}{2X_qX_d}\sin 2\delta\right) \quad (17)$$

Equation (17) indicates that the salient pole machine output power is a combination of excitation and reluctance power. Therefore at zero excitation, the salient pole machine output is purely due to the reluctance power. The maximum permissible load angle value (δ_{max}) at which maximum power is achieved is obtained by differentiating (17) with respect to the load angle (δ).

$$\frac{dP_0}{d\delta} = 3\left(\frac{V_t E_F \cos\delta}{X_d} + \frac{V_t^2(X_d - X_q)}{X_qX_d}\cos 2\delta\right) = 0 \quad (18)$$

Solving (18) quadratically gives rise to the expressions for the load angle at which maximum power is attained as shown in (19) and (20).

$$\cos\delta_{12} = \frac{-E_f \pm \sqrt{E_f^2 + 2V^2\left(\frac{X_d - X_q}{X_q}\right)^2}}{4V\left(\frac{X_d - X_q}{X_q}\right)} \quad (19)$$

$$\delta_{12} = \cos^{-1}\left(\frac{-E_f \pm \sqrt{E_f^2 + 2V^2\left(\frac{X_d - X_q}{X_q}\right)^2}}{4V\left(\frac{X_d - X_q}{X_q}\right)}\right) \quad (20)$$

The waveforms for load angle δ_{12} at varied excitation voltage and dq-axes reactances are given in figures 23 and 24.

2.1 EXCITATION SYSTEM IN SYNCHRONOUS MACHINE

Excitation system is widely used to provide a direct current to the synchronous machine field winding. This process helps in the control of generators action. The commonest generator in use today is the field excited generator [14]. The field excitation can be achieved through brushes for low power generators or brushless for high power alternators [15]. The field windings which produce the primary d.c fluxes are usually placed on the rotor since it has to sustain only a small fraction of the armature current [16]. In situations where the load on the generator changes, the excitation system is always adjusted so that a constant voltage supply and a well-controlled reactive power is

maintained. [17]. Synchronous machine excitation system can be classified into three major groups based on the source of power supply. Basically, the d.c excitation, a.c excitation and static excitation systems are the most industrially applied excitation methods in use [18]. The d.c excitation system provides the d.c current to the rotor of the synchronous machine through the slip rings. The exciter can be driven by a motor or shaft of a generator [19]. In a.c excitation system, the direct current needed for the generator field is produced through rectification by the controlled thyristor rectifiers or uncontrolled diode rectifiers. Currently, stationary and rotating a.c rectifier systems are widely used in a.c excitation system. In stationary rectifiers, the d.c output is fed to the field winding of the generator through the slip rings [20]. The d.c supply in this regard is directly fed to the generator field at the armature terminal of the exciter while the rectifiers rotate with the generator field. This excitation system is technically called the brushless d.c excitation system and was developed to avoid the problems of sparks and deteriorating brushes when an extremely high field current is applied [21]. The static excitation systems provide the synchronous generator field with d.c excitation current by means of slip rings. The rectifiers in static excitation system derive the power supply from auxiliary windings or through a stepped down transformer. Stationed batteries sometimes are used as additional power sources to this system and this can be achieved through field flashing [22].

III. METHODOLOGY: DYNAMIC MODELING OF SALIENT POLE SYNCHRONOUS MACHINE

This section presents the dynamic equations of three phase salient pole synchronous machine applied in computer simulation. The electrical and electromechanical behaviour of most synchronous machines can be predicted from the dynamic equations that describe the three phase salient pole synchronous machine [23-25]. A summary of the dynamic equations for the synchronous machine in the rotor qdo reference frame with all the rotor quantities referred to the stator is lucidly elaborated in references [26-28]. The qdo voltage equations of a synchronous machine are clearly presented in equations (21) – (27).

$$V_{qs} = r_s i_{qs} + P\lambda_{qs} + \omega_r \lambda_{ds} \quad (21)$$
$$V_{ds} = r_s i_{ds} + P\lambda_{ds} - \omega_r \lambda_{qs} \quad (22)$$
$$V_{os} = r_s i_{os} + P\lambda_{os} \quad (23)$$
$$V'_F = r'_F i'_F + P\lambda'_F \quad (24)$$
$$V'_{kd} = r'_{kd} i'_{kd} + P\lambda'_{kd} \quad (25)$$
$$V'_g = r'_g i'_g + P\lambda'_g \quad (26)$$
$$V'_{kq} = r'_{kq} i'_{kq} + P\lambda'_{Fq} \quad (27)$$

The flux linkages equations are presented in equations (28) – (34).

$$\lambda_{qs} = L_q i_{qs} + L_{mq} i'_g + L_{mq} i'_{kq} \quad (28)$$
$$\lambda_{ds} = L_d i_d + L_{md} i'_F + L_{md} i'_{kd} \quad (29)$$
$$\lambda_o = L_{Ls} i_o \quad (30)$$
$$\lambda'_F = L_{md} i_{ds} + L_{md} i'_{kd} + L'_{FF} i'_F \quad (31)$$
$$\lambda'_{kd} = L_{md} i_{ds} + L_{md} i'_{kd} + L'_{kdkd} i'_{kd} \quad (32)$$
$$\lambda'_g = L_{mq} i_{qs} + L_{mq} i'_{kq} + L'_{gg} i'_g \quad (33)$$
$$\lambda'_{kq} = L_{mq} i_{qs} + L_{mq} i'_g + L'_{kqkq} i'_{kq} \quad (34)$$

The various leakage inductances and the mutual inductances are related by equations (35) – (40).

$$L_q = L_{Ls} + L_{mq} \quad (35)$$
$$L_d = L_{Ls} + L_{md} \quad (36)$$
$$L'_{FF} = L_{LF} + L_{md} \quad (37)$$
$$L'_{kdkd} = L_{Lkd} + L_{md} \quad (38)$$
$$L'_{gg} = L_{Lg} + L_{mq} \quad (39)$$
$$L'_{kqkq} = L_{Lkq} + L_{mq} \quad (40)$$

Substituting equations (35) – (40) into equations (28) – (34) gives rise to the modified flux linkage equations represented in (41) – (46).

$$\lambda_{qs} = L_{Ls} i_{qs} + L_{mq}(i_{qs} + i'_g + i'_{kq}) \quad (41)$$
$$\lambda_{ds} = L_{Ls} i_{ds} + L_{md}(i_{ds} + i'_F + i'_{kd}) \quad (42)$$
$$\lambda'_F = L'_{LF} i'_F + L_{md}(i_{ds} + i'_F + i'_{kd}) \quad (43)$$
$$\lambda'_{kd} = L'_{Lkd} i'_{kd} + L_{md}(i_{ds} + i'_F + i'_{kd}) \quad (44)$$
$$\lambda'_g = L'_{Lg} i'_g + L_{mq}(i_{qs} + i'_g + i'_{kq}) \quad (45)$$
$$\lambda'_{kq} = L'_{Lkq} i'_{kq} + L_{mq}(i_{qs} + i'_g + i'_{kq}) \quad (46)$$

Figure 8 depicts the qdo equivalent circuits representation of the synchronous machine that is based on the above sets of voltage and flux linkage equations.

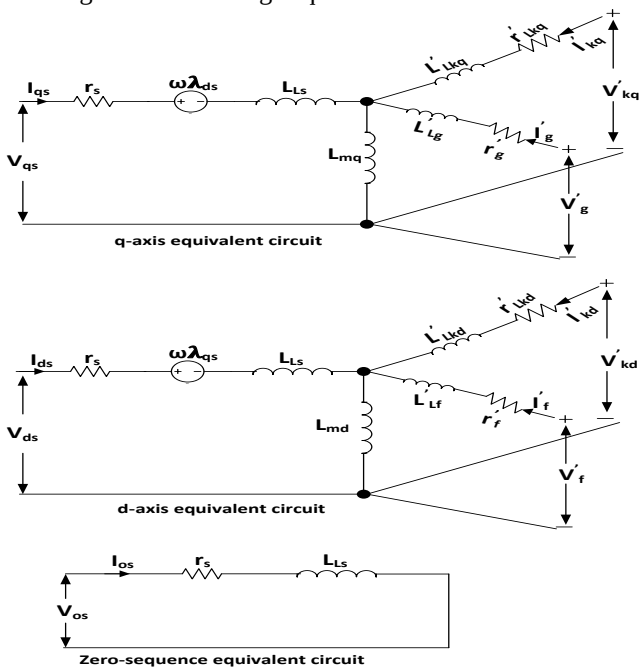

Figure 8: qdo dynamic state equivalent circuit of salient pole synchronous machine.

The electromechanical power output developed is given by equation (47).

$$P_{em} = \frac{3}{2}\left(\omega_r(\lambda_d i_{qs} - \lambda_q i_{ds})\right) \quad (47)$$

Where ω_r stands for the electrical speed which is related to the mechanical speed by equation (48).

$$\omega_r = \left(\frac{P}{2}\right)\omega_m \quad (48)$$

Substituting equation (48) into (47) gives rise to equation (49)

$$P_{em} = \frac{3}{2}\times\frac{P}{2}\times\omega_m\left(\lambda_d i_{qs} - \lambda_q i_{ds}\right) \quad (49)$$

For computer simulation purposes, the real and reactive power developed by the machine is given by equations (50) and (51).

$$P = V_{qs}i_{qs} + V_{ds}i_{ds} \quad (50)$$

$$Q = V_{qs}i_{ds} - V_{ds}i_{qs} \quad (51)$$

The electromechanical torque developed is given by equation (53).

$$T_{em} = \frac{3}{2}\times\frac{P}{2}\left(\lambda_d i_{qs} - \lambda_q i_{ds}\right) \quad (52)$$

Motor speed is derived from the motional torque and represented in (53) while the angular position is given by (54).

$$\frac{d\omega_{mr}}{dt} = \frac{1}{J}\left(T_{em} - T_{Load} - B\omega_{mr}\right) \quad (53)$$

$$\theta_r = \int_0^t \omega_{mr}\ dt \quad (54)$$

IV. RESULTS AND DISCUSSION

The simulation results were achieved with the parameters presented in Table 1. The simulation results are based on the steady state power equations and dynamic models earlier presented for the cylindrical rotor and salient pole synchronous machines. Algorithm for the digital simulation of the salient pole machine is shown in Figure 9, while a closed loop control arrangement used in the simulation for the speed control of the synchronous machine under a varying load condition is presented in Figure 10. In this closed loop, a reference speed was summed with the actual tachometer sensed machine speed to produce a speed error. The speed error generated is adjusted with a proportional integral controller to reduce the magnitude of error produced relative to the reference speed. A torque limiter that regulates the torque amplitude is connected. The output of the torque limiter is converted to a three phase current through a gain-block. The dq-currents produced are transformed to the time varying abc phase current that is applied in the modulating signal of the pulse-width modulator to generate the switching signals for the three phase inverter. The detailed analyses of the Inverter control and its firing sequences have been presented in references [29-31]..

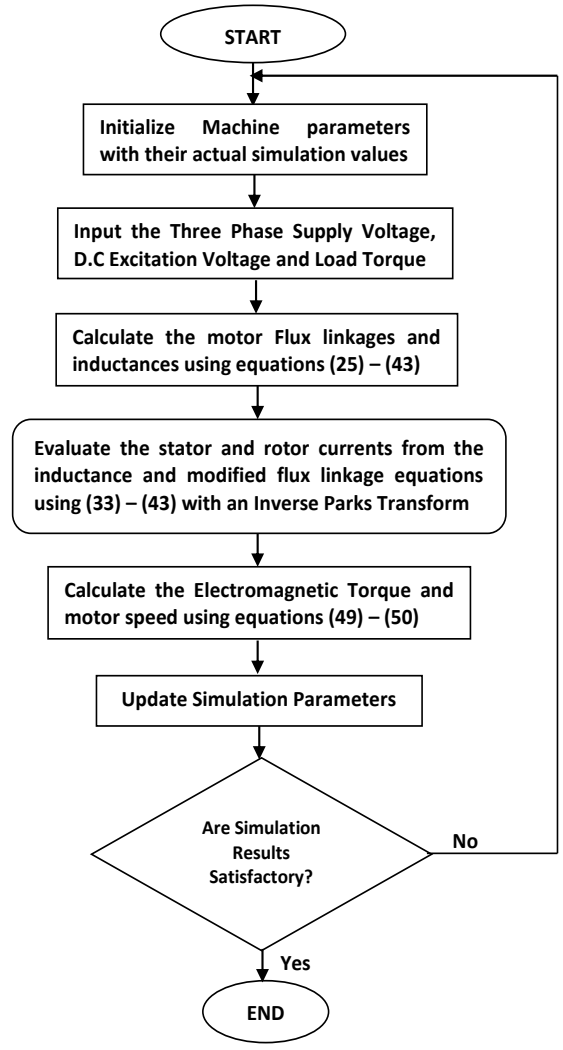

Figure 9 Algorithm for the Simulation of Salient pole Synchronous Machine

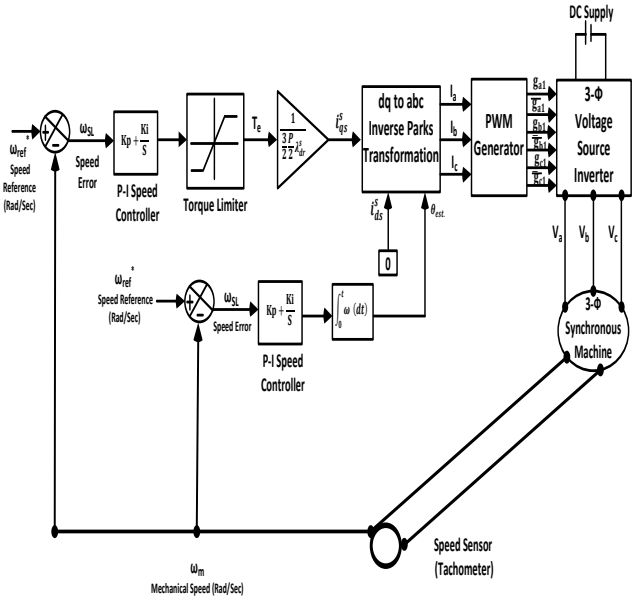

Figure 10: A block diagram for an inverter controlled synchronous machine.

Table 1: Simulation Parameters [26].

Parameters	Values
Supply Voltage V_s (V)	400
Supply Frequency F_s (Hz)	50
Rated power of the machine (KW)	400
No of Poles P	6
Expected Synchronous Speed (RPM) or Rad/Sec.	1000 or 104.73
d-axis mutual inductance L_{md} (H)	0.01686
q-axis mutual inductance L_{mq} (H)	0.01447
Stator winding leakage inductance L_{Ls} (H)	0.00076
Field winding leakage inductance L_{Lfr} (H)	0.0075
Rotor q-axis leakage inductance L_{Lqr} (H)	0.0011
Rotor d-axis leakage inductance L_{Ldr} (H)	0.0011
Rotor q-axis winding resistance R_{qr} (Ω)	2.916
Rotor d-axis winding resistance R_{dr} (Ω)	2.916
Stator winding resistance R_s (Ω)	0.0738
Rotor field winding resistance R_{Fr} (Ω)	0.434
d-axis damper leakage inductance L'_{Lkd} (H)	0.0057
q-axis damper leakage inductance L'_{Lkq} (H)	0.0057
d-axis damper resistance R'_{kd} (Ω)	0.7324
q-axis damper resistance R'_{kq} (Ω)	1.6230
Field excitation voltage under steady state E_F (V)	5, 7.5, 10, 12.5
Field excitation voltage under dynamic state V_{Fr} (V)	24 and 72
Moment of Inertia J (Kgm^2)	0.36233
Range of Load angle δ (degrees)	0 to 180
Applied Load Torque TL (Nm)	0 and 50

The simulation results presented in Figures 11-14 under steady state condition showed that the excitation power remained unchanged as the quadrature axis reactance X_q varied correspondingly with direct axis reactance X_d for $X_q = 0.5X_d$, $0.65X_d$, $1.75X_d$ and $2.25X_d$ at constant excitation voltage of $E_F = 5V$. Power due to saliency decreased from 137.2W to 97.46W at $X_q = 0.5X_d$ and $0.65X_d$ as shown in Figures 11 and 12 respectively. In Figures 13 and 14, a sharp increase in salient power from 114.7W to 166.2W was obtained for $X_q = 1.75X_d$ and $2.25X_d$ with a constant excitation power value of 84.1W and constant excitation voltage of $E_F = 5V$. Conversely, at a varied excitation voltage, a rapid increase in excitation power of [P_{E1} = 167.6W; P_{E2} = 251.4W; P_{E3} = 335.2W; P_{E4} = 419.1W] was obtained as shown in Figure 15. This increase in power corresponded with the sequential rise in the excitation voltage of [$E_{F1} = 5V$; $E_{F2} = 7.5V$; $E_{F3} = 10V$; $E_{F4} = 12.5V$]. Similarly, the rise in salient power in the sequence of [P_{T1} = 210.9W; P_{T2} = 284.5W; P_{T3} = 364.7W; P_{T4} = 444.8W] was achieved in Figure 16 which is slightly above the excitation power under the same rise in voltage excitation and q-axis reactance value of $X_q = 0.5X_d$. In Figure 17, as the quadrature axis reactance is set at $X_q = 0.75X_d$ under a varied excitation voltage, it is observed that the sequence of increase in excitation power remained unchanged and is the same as that obtained in Figure 15. In Figure 18, a sharp decrease in the salient power was obtained when $X_q = 0.75X_d$ as compared to when $X_q = 0.5X_d$. In Figure 19, at $X_q = 1.75X_d$ and varied excitation voltage, the variation in the excitation power remained unchanged while the power output due to saliency in Figure 20 slightly increased as compared to the values obtained in Figure 18. At $X_q = 2.25X_d$, the peak value of the excitation power still remained unchanged as shown in Figure 21 while a sharp variation in the output power due to saliency was obtained in the sequence of [P_{T1} = 236.2W; P_{T2} = 309.1W; P_{T3} = 382.1W; P_{T4} = 462.2W] as presented in Figure 22. This implies that the power due to saliency for a salient pole synchronous machine is grossly affected by the quadrature axis reactance while the excitation power obtained from the cylindrical rotor is independent of quadrature axis reactance but on the magnitude of the d.c excitation voltage as buttressed in equation (17). The load angle plots of equation (20) presented in Figure 23 shows that the load angle decreases as the excitation voltage increases at a varied quadrature axis reactance under a motoring mode of machine operation. Conversely, in Figure 24 when the machine operates as a generator, the load angle increases proportionately with the increase in excitation voltage at varied quadrature axis reactance in accordance with equation (20).

The simulation results under dynamic state characteristics are presented in Figures 25-40 respectively. The d-q axes stator flux linkages are shown in Figure 25 at constant excitation voltage of $E_F = 24V$. At start, there was a transient oscillation. On attainment of full speed, the d-axis flux linkage $\boldsymbol{\lambda}_{ds}$ became zero on no-load synchronous speed and attained a value of 0.524 V/sec on full load. The q-axis flux linkage $\boldsymbol{\lambda}_{qs}$ assumed a no-load value of 1.71V/sec and on rated load torque, it settled to 1.445 V/sec. The zero axis flux linkage assumed a zero value throughout the simulation period. Similarly, with an increased excitation voltage to 72V, the transient period became prolonged. The d-axis flux linkage $\boldsymbol{\lambda}_{ds}$ still remained zero on no-load but attained a value of 0.175 V/sec on full load. The q-axis flux linkage $\boldsymbol{\lambda}_{qs}$ assumed a no-load value of 1.71 V/sec with no appreciable change on application of full load torque as shown Figure 26. The three phase stator currents $\mathbf{I_{as}}$, $\mathbf{I_{bs}}$ and $\mathbf{I_{cs}}$ plotted against time is shown in Figure 27. The currents are seen to be visibly high at starting but settles down to the rated no-load current of 13.3A per phase. On application of the rated load torque, the current rapidly rose and settled at 35.5A. In Figure 28, at an increased excitation voltage of 72V, it is observed that the rise in current oscillation is higher at starting on no-load but attained steady state after 0.5second and finally settled down to 28.5A on full load. The three phase rotor currents plotted in Figure 29 shows a rise in transient oscillation at a simulation period of 0-0.5second. On attainment of full speed, the rotor currents I_{dr} and I_{qr} became zero while the field current I_{fr} remained at 28.4A. At an increased excitation voltage of 72V and full speed, the rotor currents I_{dr} and I_{qr} remained at zero value but the field current rapidly increased to 195.4A as shown in Figure 30. The real and reactive power outputs were plotted in Figure 31 at an excitation voltage of 24V. It is observed that the transient was very high at start. After the machine has

attained full speed, the real power became zero on no-load synchronous speed and attained a value of 0.85KW (0.085×10^4W) on full load. Similarly, the reactive power settled at 1.5KVAR (0.15×10^4VAR) on no-load and rose to 1.8KVAR (0.18×10^4VAR) on full load. In Figure 32, at an excitation voltage of 72V, it is observed that there was a strong oscillation in the real power at the start of the simulation which decreased to zero value on no-load at synchronous speed. At full load condition, the real power increased from zero value to 15KW (0.15×10^5W) under a steady state synchronous speed. Similarly, a rapid change in the value of the reactive power was observed as shown in Figure 32. An absolute peak value of $|-0.375 \times 10^5| = 37.5$ KVAR indicates that much current was drawn by the machine as the excitation voltage is increased to 72V. In Figure 33 which represents the rotor flux linkages shows that the d-axis rotor flux linkage $\boldsymbol{\lambda}_{dr}$ was zero on no-load but rose to 0.467 V/sec on application of rated load torque. The q-axis rotor flux linkage $\boldsymbol{\lambda}_{qr}$ settled at 1.695 V/sec on no-load after all transients have disappeared and decreased to 1.467 V/sec on application of load torque. The field flux linkage had a value of 1.92 V/sec under a no-load steady state conditions and maintained a full load value of 1.87V/sec. In Figure 34, a prolonged oscillation was observed when an excitation voltage was increased to 72V for the d-axis rotor flux linkage. On full load, the d-axis rotor flux linkage slightly increased to 0.49 V/sec. The q-axis flux linkage maintained a value of 1.85 V/sec on no-load after the transient period with a slight drop in the value of 1.78 V/sec obtained on full load. At an increased field excitation voltage of 72V, the field flux linkage increased to 2.9 V/sec on no-load at the expiration of the transient period. A very slight decrease in value of 2.87 V/sec was obtained on full load synchronous speed as shown in Figure 34. The run-up speed characteristic is presented in Figure 35. It is observed that during machine starting and on no-load, there was an overshoot in speed with minor oscillations before the motor speed finally settled at 104.73 rad/sec which is equivalent to 1000rpm synchronous speed for a 6-pole, 50Hz synchronous motor. On application of 50Nm full load torque at 2.0second simulation time, the speed dropped and oscillated between 102.5 rad/sec and 105.4 rad/sec before attaining a synchronous speed of 104.73 rad/sec after 2.55 seconds. At an increased excitation voltage of 72V, a high overshoot in speed and prolonged oscillation was obtained during a no-load condition before attaining a synchronous speed value of 104.73 rad/sec as shown in Figure 36. On full load at 2.0second, a drop in speed was observed before a synchronous speed value of 104.73 rad/sec was attained at steady state. The plot of torque against time is shown in Figure 37. Torque oscillation was observed during starting which lasted for 1.25second. The torque naturally settled to a zero value on no-load. On full load application, the motor torque rose to 99.5Nm at 2.0 second and settled at a a value of 56.467Nm in 2.56 seconds. In Figure 38, it is shown that at an increased excitation voltage of 72V, a prolonged oscillation in torque was observed before a zero value was obtained on no-load synchronous speed. On full load, the torque rose to 89.5Nm before attaining a steady state value of 54.36Nm at 2.5second. In Figure 39, the torque-speed characteristic was presented. It is observed that the high value of torque at low speed decreased proportionately as the speed value increased which is in conformity with all electrical machine characteristics. The curl in Figure 39 settled at 104.73 rad/sec which corresponded to the synchronous speed value. In Figure 40, it is observed that at an increased excitation voltage of 72V, the curl for the torque speed plot enlarged and closely curved at 104.73 rad/sec on full load synchronous speed.

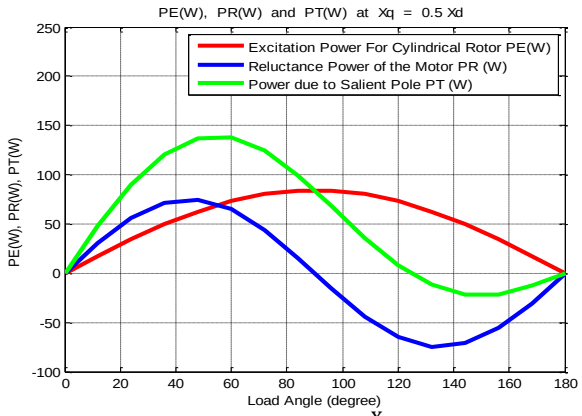

Figure 11: Power & Load Angle at $\frac{X_q}{X_d} = 0.5$ & $E_F = 5V$

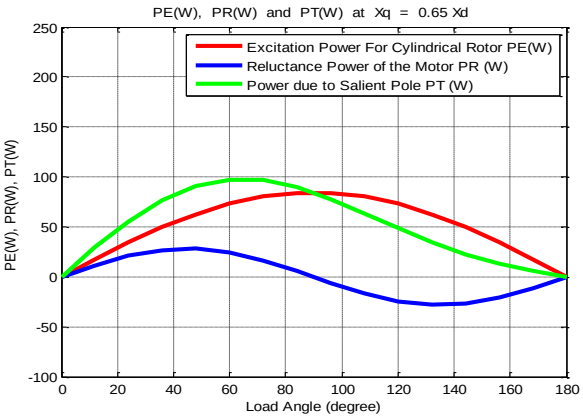

Figure 12: Power & Load Angle at $\frac{X_q}{X_d} = 0.65$ & $E_F = 5V$

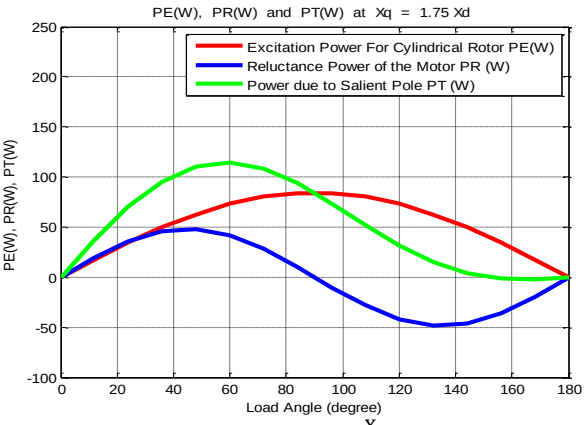

Figure 13: Power & Load Angle at $\frac{X_q}{X_d} = 1.75$ & $E_F = 5V$

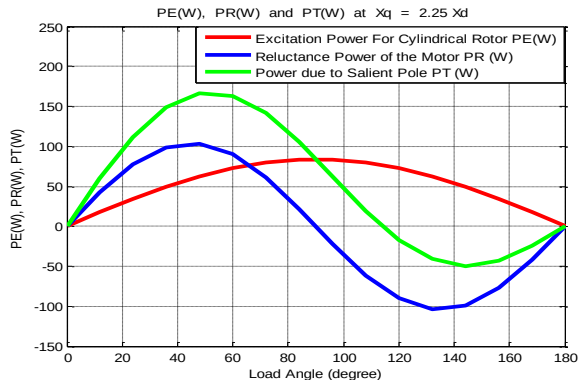

Figure 14: Power & Load Angle at $\frac{X_q}{X_d} = 2.25$ & $E_F = 5V$

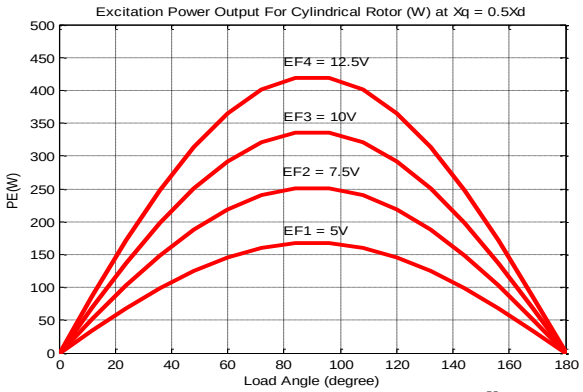

Figure 15:Excitation power & Load Angle at $\frac{X_q}{X_d} = 0.5$

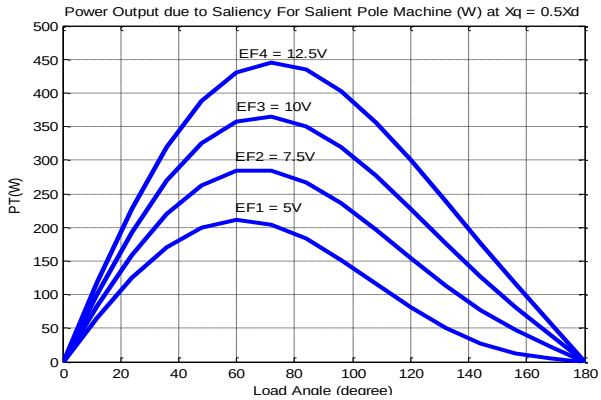

Figure 16:Salient power & Load Angle at $\frac{X_q}{X_d} = 0.5$

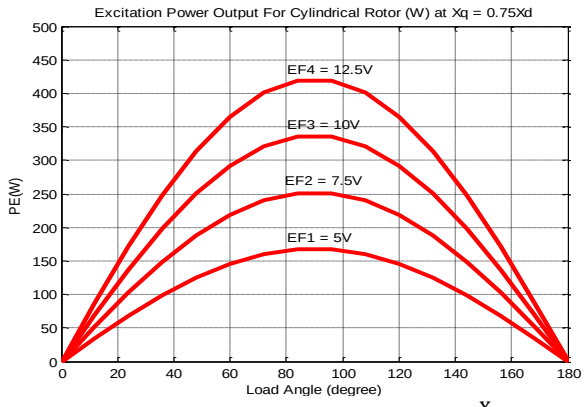

Figure 17:Excitation power & Load Angle at $\frac{X_q}{X_d} = 0.75$

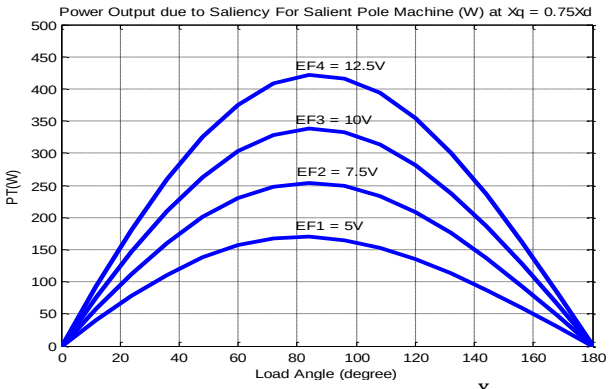

Figure 18:Salient power & Load Angle at $\frac{X_q}{X_d} = 0.75$

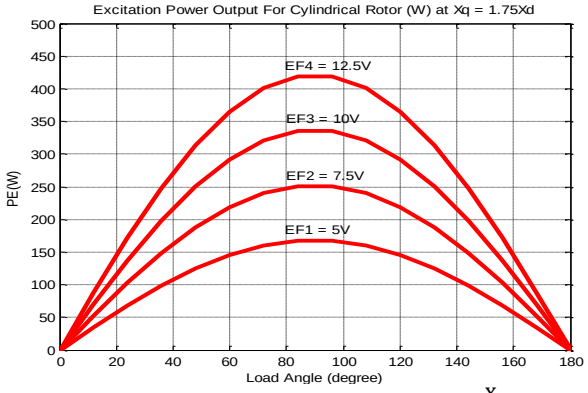

Figure 19:Excitation power & Load Angle at $\frac{X_q}{X_d} = 1.75$

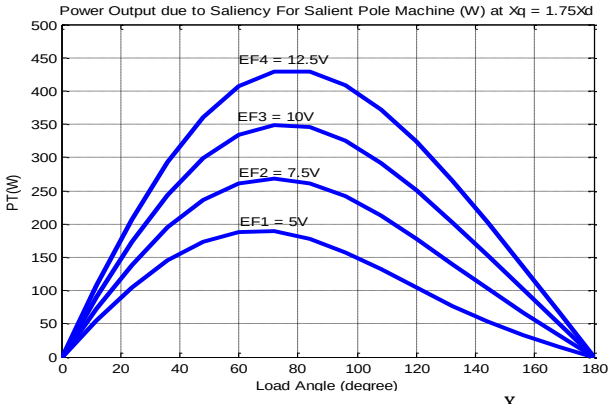

Figure 20:Salient power & Load Angle at $\frac{X_q}{X_d} = 1.75$

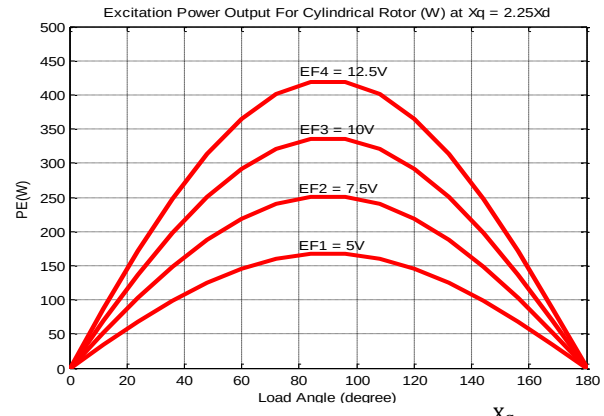

Figure 21:Excitation power & Load Angle at $\frac{X_q}{X_d} = 2.25$

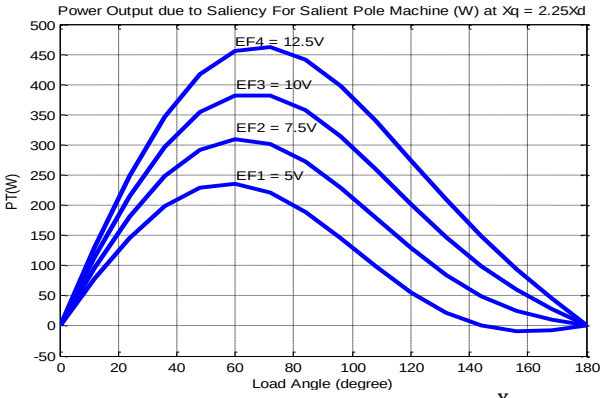

Figure 22:Salient power & Load Angle at $\frac{X_q}{X_d} = 2.25$

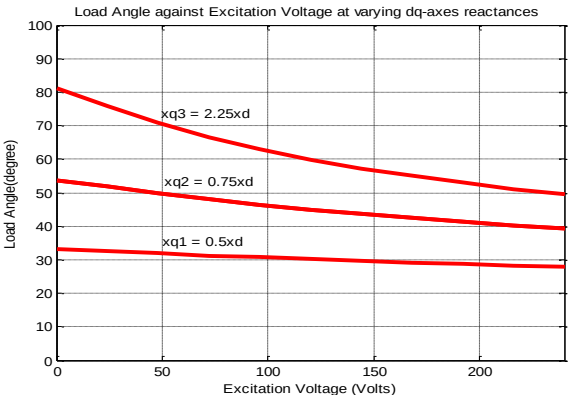

Figure 23: Load angle (δ_1) against Excitation Voltage

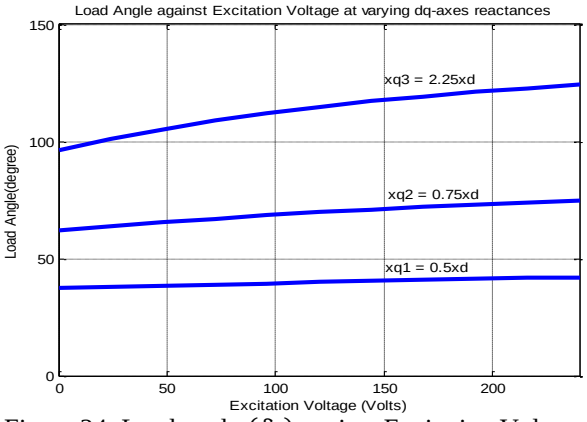

Figure 24: Load angle (δ_2) against Excitation Voltage

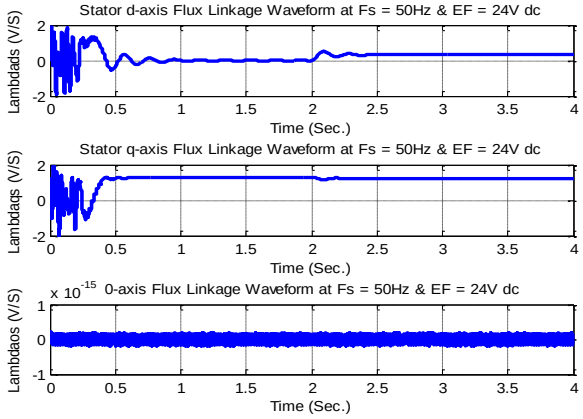

Figure 25: $\lambda_{ds}\lambda_{qs}\lambda_{os}$ against Time at EF = 24V

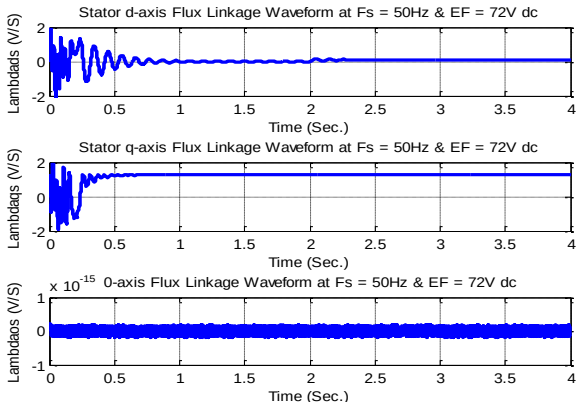

Figure 26: $\lambda_{ds}\lambda_{qs}\lambda_{os}$ against Time at EF = 72V

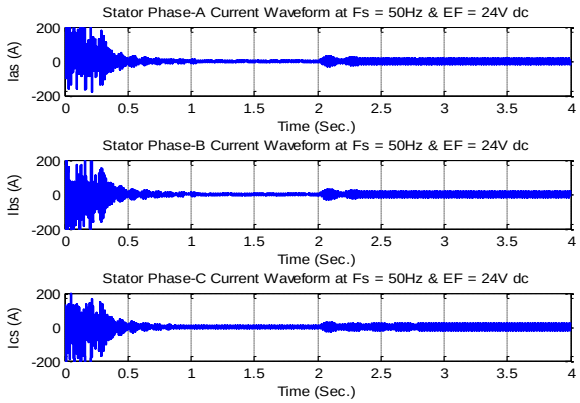

Figure 27: $I_{as}I_{bs}I_{cs}$ against Time at EF = 24V

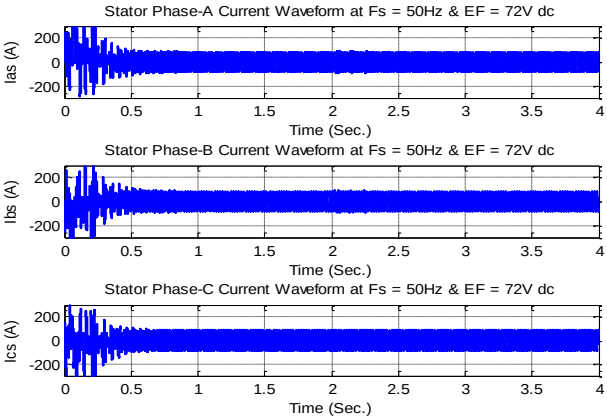

Figure 28: $I_{as}I_{bs}I_{cs}$ against Time at EF = 72V

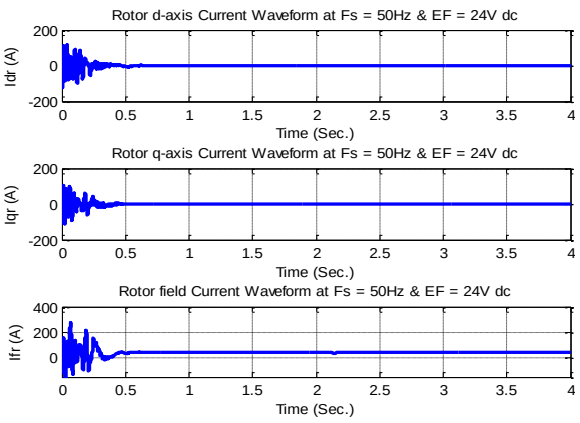

Figure 29: $I_{dr}I_{qr}I_{fr}$ against Time at EF = 24V

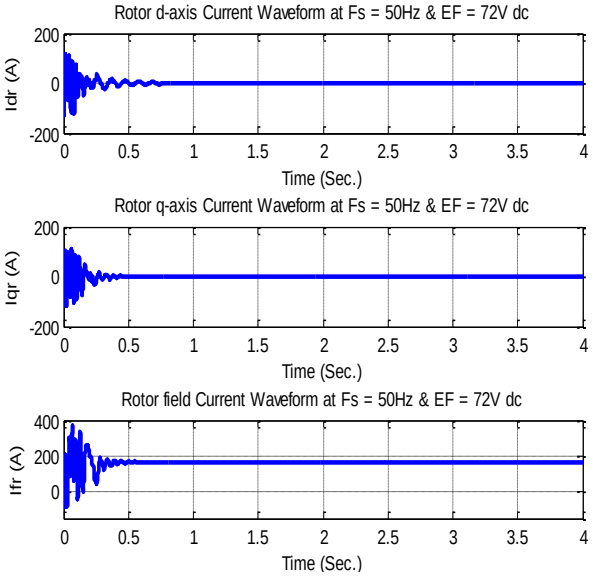

Figure 30: $I_{dr}I_{qr}I_{fr}$ against Time at EF = 72V

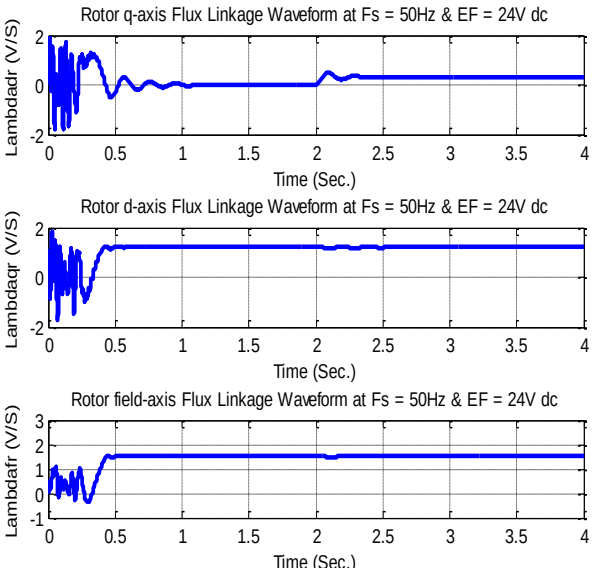

Figure 33: $\lambda_{dr}\lambda_{qr}\lambda_{fr}$ against Time at EF = 24V

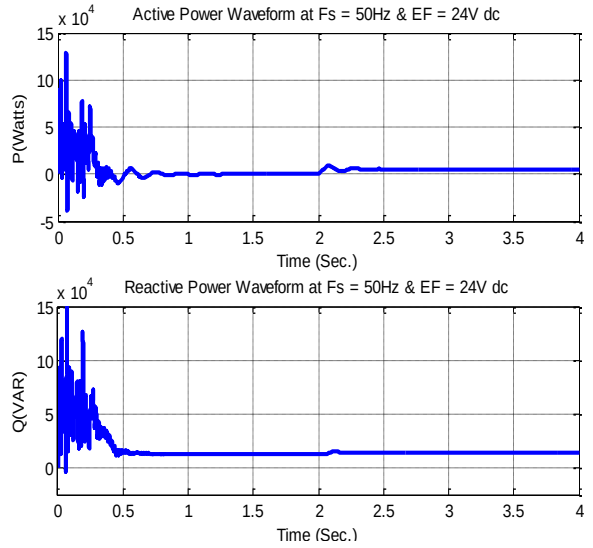

Figure 31: PQ against Time at EF = 24V

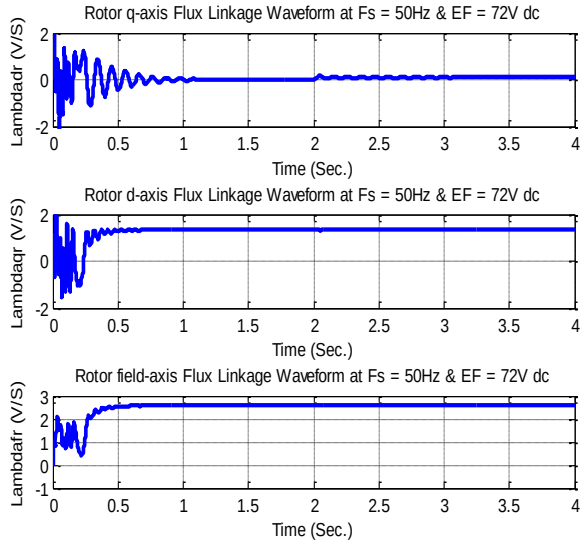

Figure 34: $\lambda_{dr}\lambda_{qr}\lambda_{fr}$ against Time at EF = 72V

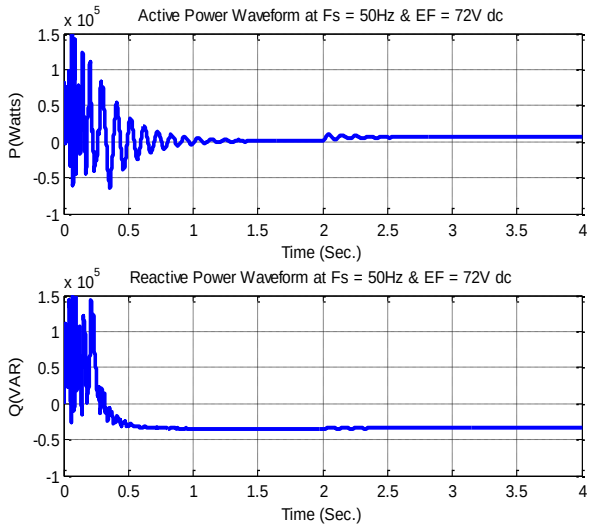

Figure 32: PQ against Time at EF = 72V

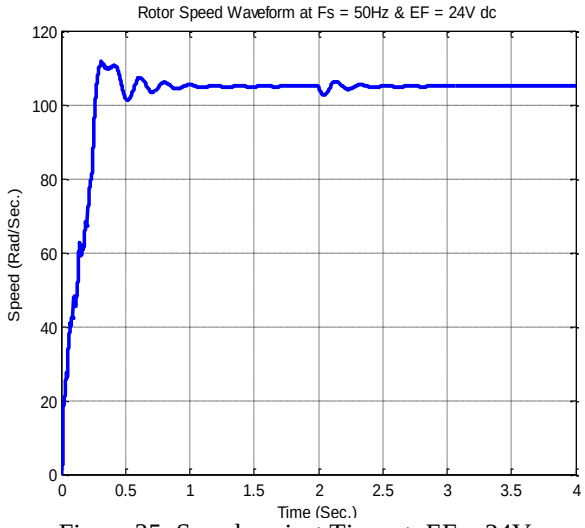

Figure 35: Speed against Time at EF = 24V

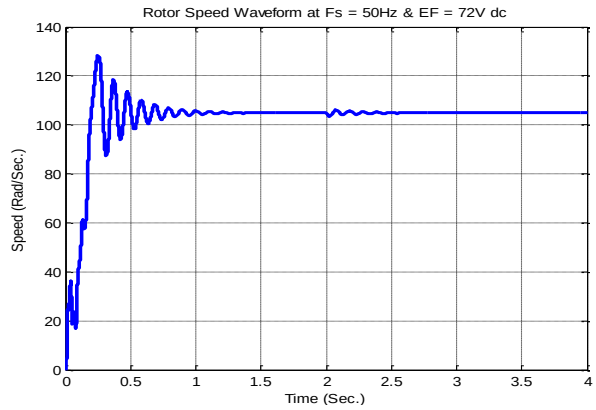

Figure 36: Speed against Time at EF = 72V

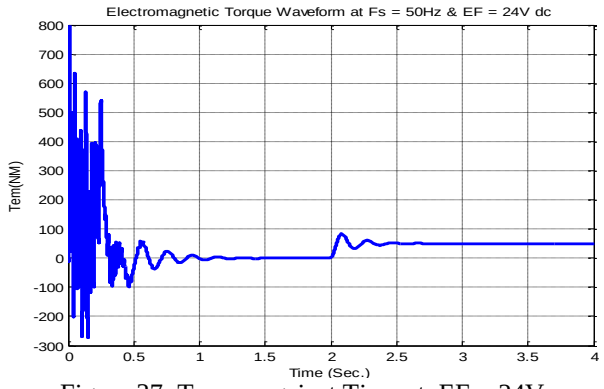

Figure 37: Torque against Time at EF = 24V

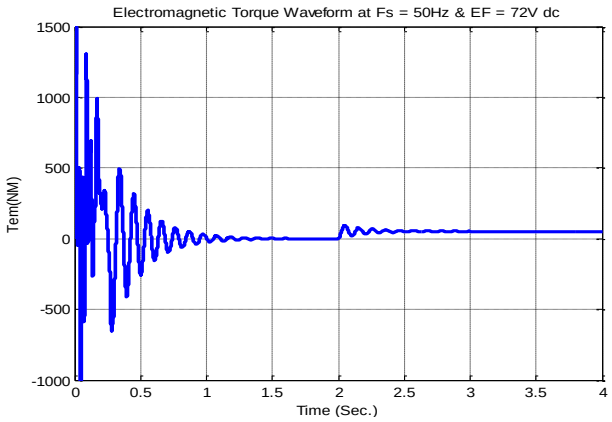

Figure 38: Torque against Time at EF = 72V

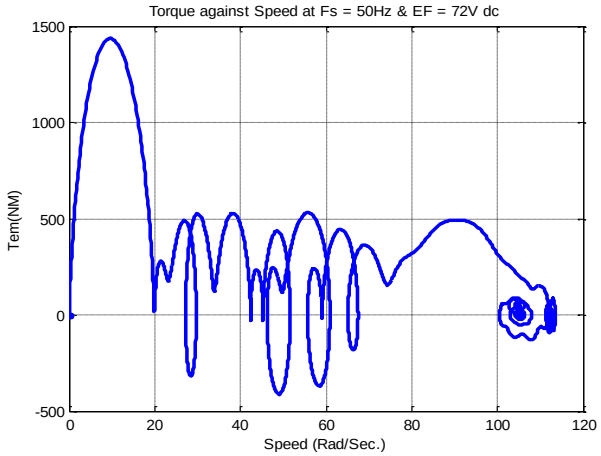

Figure 39: Torque against Speed at EF = 24V

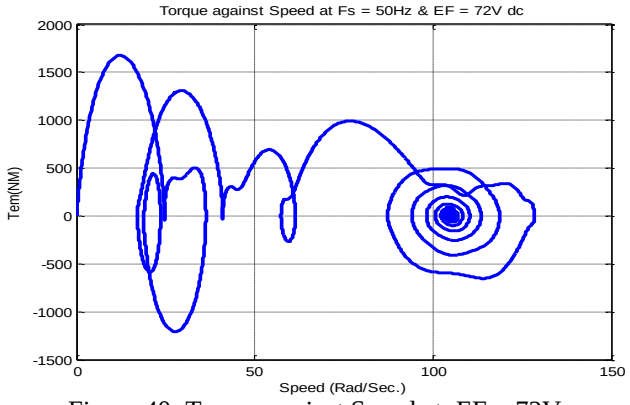

Figure 40: Torque against Speed at EF = 72V

The results obtained when a three phase to ground fault was introduced at a simulation period of 4.0-4.5seconds and excitation voltage of 24V are presented in figures 41-48 respectively. It is observed in Figure 41 that at the instant of fault occurrence, the dqo-axes flux linkages became zero and rapidly oscillated on fault clearance. The d-axis flux linkage λ_{ds} oscillated from -1.71 V/sec to $+1.85$ V/sec at the moment of fault removal. At a simulation period of 6.04Seconds, the flux linkage attained a steady state value of 0.524 V/sec through out the simulation period. Similarly, the q-axis flux linkage λ_{qs} on faults clearance oscillated from -1.69 V/sec to $+1.87$ V/sec but attained a steady state value of $+1.44$ V/sec at 6.04 seconds. The zero axis flux linkage λ_{os} assumed a zero value during fault and maintained a value of $+0.075$ V/sec on fault removal. In Figure 42, a rapid drop in the three phase stator current was observed during fault. On fault removal, a sharp rise in current value was obtained which attained a steady state value of 75.5A throughout the simulation time. In Figure 43, the dq-axes current and the field current maintained a zero value during the fault period. At the instant of fault clearance, a rapid oscillation was observed and a steady state value of 5.5A was obtained for the dq-axes current while the field current maintained a steady state value of 56.8A after 6.04Second. In Figure 44, the real and reactive power became zero during the fault period. On fault clearance, the transient in the real and reactive power became very high. A steady state value of 0.85kW was obtained for the real power while the reactive power maintained a steady state value of 0.45KVAR after 6.04 Seconds. In Figure 45, a sharp drop in the value of the dq-axes flux linkage and field flux linkage was observed at the instant of fault. The dq-axes flux linkage maintained a zero value at 4.25second. A high transient oscillation was observed on faults removal while a steady state value was attained after 6.04second simulation time. In Figure 46, a drastic drop in speed from 104.73 rad/sec to 21.85 rad/sec was obtained at the instant of fault. On fault clearance, a gradual rise in speed was observed which attained a steady state value of 104.73 rad/sec after 6.0 second. In Figure 47, a pronounced drop in electromechanical torque which reduced to a zero value was observed during fault. On fault removal, a rapid transient occurred. This was attenuated after few seconds before a steady state value of 99.5Nm

was obtained after 6.0second. The characteristics waveforms of the torque against speed is depicted in Figure 48. It is obvious that the distorted curl with a pronounced transient oscillation is a consequence of a three phase to ground fault.

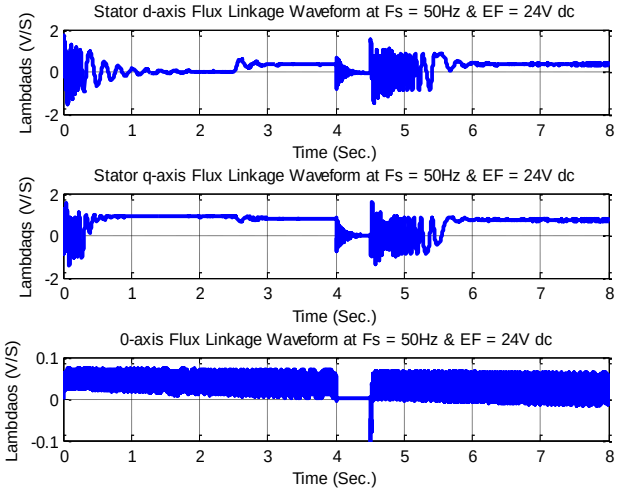

Figure 41: $\lambda_{ds}\lambda_{qs}\lambda_{os}$ against Time at EF = 24V

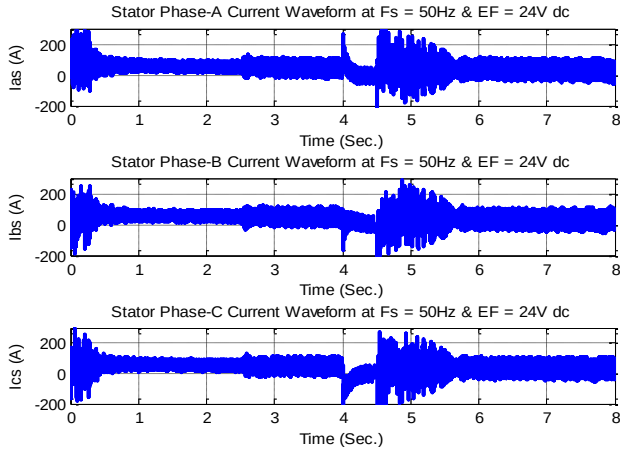

Figure 42: $I_{as}I_{bs}I_{cs}$ against Time at EF = 24V

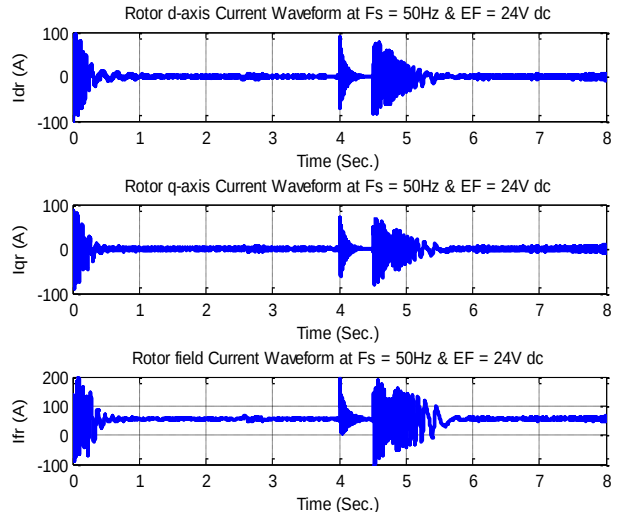

Figure 43: $I_{dr}I_{qr}I_{fr}$ against Time at EF = 24V

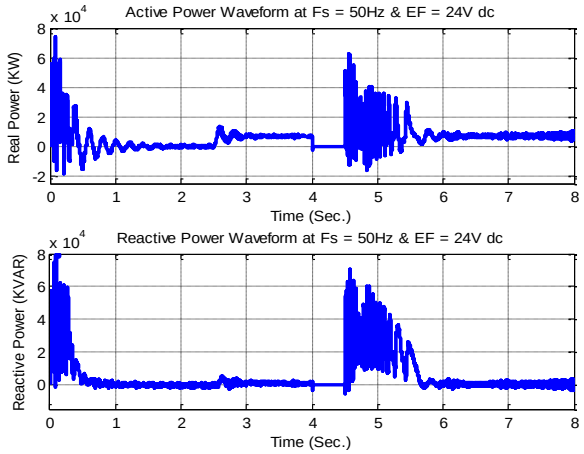

Figure 44: PQ against Time at EF = 24V

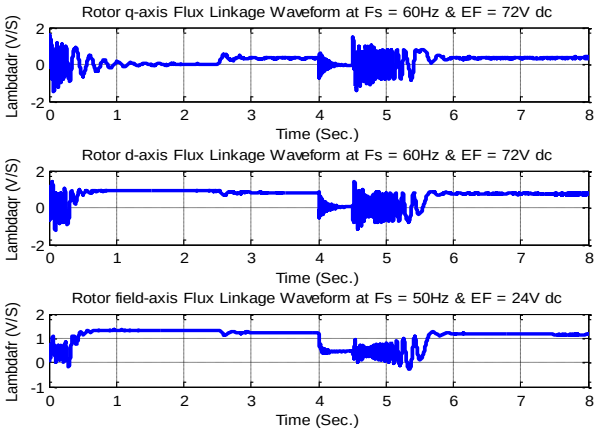

Figure 45: $\lambda_{qr}\lambda_{dr}\lambda_{fr}$ against Time at EF = 24V

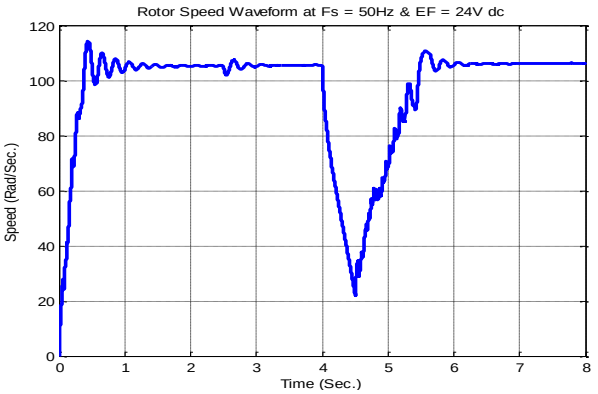

Figure 46: Speed against Time at EF = 24V

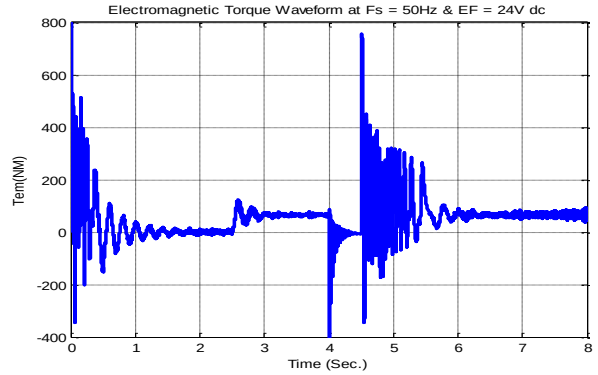

Figure 47: Torque against Time at EF = 24V

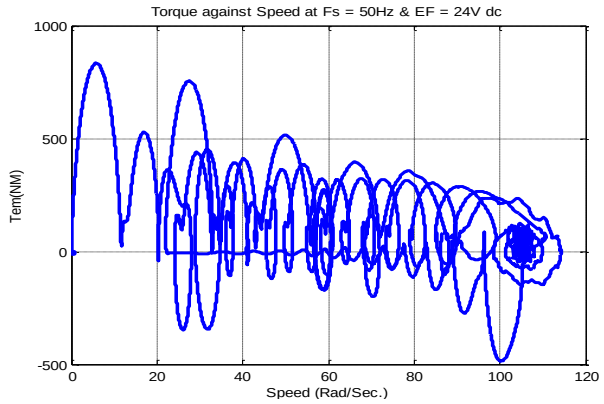

Figure 48: Torque against Speed at EF = 24V

V. CONCLUSION

In this paper, comparisons were drawn in the performance of two selected synchronous machines through computer simulation under a varying q-axis reactance and field excitation voltage. The results obtained indicated that the salient pole synchronous machine generated a higher output power than the counterpart cylindrical rotor machine at constant excitation voltage and varied q-axis reactance. The rise in the power output of the cylindrical rotor machine (excitation power) increased with the excitation voltage but remained constant as the q-axis reactance increased. Similarly, the rise in the power output of the salient pole machine varied correspondingly with the rise in the q-axis reactance and field excitation voltage. Simulation results showed that a zero excitation voltage reduced the excitation power of the cylindrical rotor machine to zero value but did not entirely reduce the power developed by the salient pole to zero due to saliency. The results obtained at a varied reactance value showed that a considerable difference in the magnitude of the peak output power for the salient pole machine was achieved. The dynamic state simulation results for the 6-pole 50Hz salient pole machine showed that at a varied field excitation voltage of 24V and 72V, there was a visible rise in current value. This variation in the field excitation voltage affected the machine power factor characteristics. This is shown in the rise of real and reactive power values from 0.85KW to 15KW and 1.8KVAR to 37.5KVAR (lagging). It is also evident that the rise in the field current from 28.4A to 195.4A at an increased excitation voltage of 72V is a good pointer for machine designers in varying machine power factor. Most importantly, this paper has analyzed the rate of torque and speed pulsations inherent in a three phase synchronous machine during steady state and dynamic operation under a severe three line to ground (3LG) fault. The rapid drop in speed value 104.73 to 21.85 rad/sec and torque value 99.5 to 0 Nm during fault necessitates a quick fault clearing device that can reduce the downtime of the synchronous machine without actually affecting its performance efficiency. It is therefore recommended that a practical work be carried out in the future for the validation of these simulation results.

REFERENCES

[1] L. Wieslaw, "Comparative Analysis of Energy Performance of Squirrel Cage Induction Motor Line-Start Synchronous Reluctance And Permanent Magnet Motors Employing The Same Stator Design," Archives of Electrical Engineering, **Vol. 69, No.4, pp. 967-981, 2020.**

[2] P. Guglielmi, et al, "Permanent Magnet Minimization In Pm-Assisted Synchronous Reluctance Motors For Wide Speed Range," IEEE Transaction on Industry applications, **Vol.49, No.1, pp. 31-41, 2013.**

[3] P.R. Viego, V. Sousa, J.R. Gomez, et al "Direct-Online Start Permanent Magnet Assisted Synchronous Reluctance Motors with Ferrite Magnets for Driving Constant Loads," International Journal of Electrical and Computer Engineering, **Vol. 10, No.1, pp.651-659, 2020.**

[4] S. Stipetic, D. Zarko, N. Cavar, "Adjustment of Rated Current and Power Factor In A Synchronous Reluctance Motor Optimally Designed For Maximum Saliency Ratio," IEEE Transactions on Industry Applications, **Vol. 56, No.3, pp. 2481-2490, 2020.**

[5] J.B. Gupta, Theory and Performance of Electrical Machines. S.K. Kataria & Sons Publisher New Delhi, **2013**.

[6] L. Albert, N. Bianchi and S. Bolognani, "High Frequency D-Q Model of Synchronous Machines for Sensor - Less Control" .IEEE Transactions on Industrial Applications **Vol. 55, No. 99, pp. 1-11, 2015.**

[7] L. Alberti, N. Bianchi, M. Morandim and J. Gyselinck, "Small-Signal Finite Element Modeling of Synchronous Machines For Sensor Less Applications". International Conference on Electrical Machines (ICEM) Marsielle France, 2nd-5th September, **pp. 2264-2270, 2012.**

[8] H. Wu, "Small-Signal Modeling and Parameter Design for Vertical Synchronous Generators." IEEE Trans.Ind. Electronics, **Vol. 63, No.7, pp. 4292-4303, 2016.**

[9] L. Alberti, N. Bianchi and S. Bolognani, "Comparison of Different Synchronous Machines For Sensor Less Drives". In 39th Annual Conference of IEEE Industrial Electronics Society (IECON) November **pp. 8220-8226, 2013.**

[10] C. Li, G. Wang, et al, "Saliency-Based Sensor less Control for Synchronous Reluctance Machine Drives with Suppression Of Position Estimation Error," IEEE Transactions on Industrial Electronics, **Vol. 66, No.8, pp. 5839-5849, 2019.**

[11] W. Chai, W. Zhao, B. Kwon, "Optimal Design of Wound Field Synchronous Reluctance Machine to Improve Torque by Increasing the Saliency Ratio," IEEE transactions on magnetics **Vol. 53, No.11, pp. 1325-1335, 2017.**

[12] V. Aguba, M. Muteba, D.V. Nicolae "Transient Analysis of a Start-Up Synchronous Reluctance Motor with Symmetrical Distributed Rotor Cage Bars," AFRICON 2017, On-line: IEEE Xplore, pp.1290-1295, DOI: 10.1109/AFRICON.2017.8095668.

[13] C.M. Spargo, et al, "Application of Fractional Slot Concentrated Windings to Synchronous Reluctance Motor," IEEE Transactions on Industry Applications, **Vol. 51, No.2, pp. 1446-1455, 2015.**

[14] A. Blanc, "Exciting Field and Quadrature Axis Armature Reaction In A Cascade Equivalent A-H Circuit of a Salient Pole Generator," International Journal of Electrical and Computer Engineering . **Vol. 10, No.2, pp.1674-1681, April, 2020.**

[15] R. Jamil, I. Jamil, Z. Jinquan, I. Ming and W.Y. Dong. "Control and Configuration of Generator Excitation System as Current Mainstream Technology of Power System". TC. **Vol. 1 No.1, p.1, 2013.**

[16] E.S. Obe, L.U. Anih and B.U. Akuru. "A Simple Excitation Control for an Isolated Synchronous Generator". Nigerian Journal of Technology (NIJOTECH) **Vol. 32, No.3, pp. 433-434, 2013.**

[17] F. Rettinger, G. Huth, "Variable Speed PM Synchronous Motors with Ferrite Excitation," Electrical Engineering, **Vol. 99, No.2, pp. 639-648, 2017.**
[18] S. Schmuelling, C. Kreischer and M. Goleblowsi, "Comparison of Different Methods for Excitation of Synchronous Machines". KOMEL **Vol. 107, pp. 89-93, 2015.**
[19] S. Tsegaye and K.A. Fante, "Analysis of Synchronous Machine Excitation Systems: Comparative Study". World Academy of Science, Engineering and Technology. International Journal of Energy and Power Engineering. **Vol. 10, No.12, pp. 1492-1496, 2016.**
[20] J. Vedrana, M. Kresimir; and Z. Spoljaric. "Excitation System Models of Synchronous generator". Faculty of Electrical Engineering Osijek, Croatia 28th International Conference on Science and Practice, **2010**.
[21] IEEE Power Engineering Society, "IEEE Recommended Practice for Excitation System Models for Power System Stability studies," IEE Std. 421-5-2005, IEEE New York, NY, USA, **2006**.
[22] B. Wojciech, P. Kielan, Z. Kowalk, "Synchronous Reluctance Machine Drive Control with Fast Prototyping Card Implementation," Archives of Electrical Engineering, **Vol. 69, No.4 pp. 757-769, 2020.**
[23] K. Paul, W. Oleg, S. Scott and P. Steven, "Analysis of Electric Machinery and Drive Systems". New Jersey: John Wiley and Sons, Inc **2013**.
[24] I. Tabatabaei, J. Faiz, H. Lesani and M.T. Nabavi-Razavi, "Modeling and Simulation of a Salient Pole Synchronous Generator with Dynamic Eccentricity Using Modified Winding Function Theory". IEEE Transaction on Magnetics, **Vol. 40, No. 3, pp. 1550-1555, 2004.**
[25] C.O. Onah, and J. Reuben, "Dynamic Modeling and Simulation of Salient Pole Synchronous Motor Using Embedded Matlab". American Journal of Engineering Research (AJER) **Vol. 5, Issue 12, pp. 318-325, 2016.**
[26] M. Mythili and K. Annapoorani, "Modeling of Salient Pole Synchronous Machine". International Journal of Advanced Research in Electrical, Electronics and Instrumentation Engineering. **Vol. 3 No. 1 pp. 197-200, 2014.**
[27] P.C. Krause, O. Wasynczuk and S.D. Sudhoff, Analysis of Electric Machinery, Piscataway: IEEE Press **2002**.
[28] C.M. Ong, Dynamic Simulation of Electric Machinery Taiwan Prentice Hall PTR, **1998**.
[29] Eya, C.U., Omeje, C.O. and Ukwejeh, J.M. Solar-powered five level output voltage of dc-ac converter using simplified capacitor voltage controlled scheme (SCVCS)." IEEE PES/IAS Power Africa Conference **pp. 464-469, 2019.**
[30] Omeje, C.O. Nnadi, D.B. and Odeh, C.I. Analysis of harmonic injection to the modulation of multilevel diode clamped converter in a normal and over modulation mode, Nigerian Journal of Technology **vol. 32, pp. 67-80, 2013.**
[31] Omeje, C.O. and Agu, M.U. Speed control of a squirrel cage induction motor with a balanced capacitor voltage fed multi-level diode clamped converter. International Journal of Engineering Research & Technology, **vol.8 issue 12, pp. 135-141, 2019.**

AUTHORS PROFILE

Crescent Onyebuchi Omeje received his Bachelor's degree in Electrical Engineering, in 2004 from University of Nigeria, Nsukka. He also obtained his Masters of Engineering (M.Eng) and Doctor of Philosophy (Ph.D) with distinction in 2011 and 2019 respectively in Electrical Engineering, from the same University. He is a Member of Nigeria Society of Engineers (MNSE), a registered member Council for the regulation of Engineering in Nigeria (COREN), a member of the Institute of Electrical/Electronic Engineering (IEEE) and a full-time lecturer in the Department of Electrical/Electronic Engineering, University of Port Harcourt, Rivers State, Nigeria. His research interests are on power electronics, new energy conversion systems, multilevel inverter applications, smart grid intelligent systems, and Electric motor drives. email:crescent.omeje@uniport.edu.ng

Stephen Ejiofor Oti received a B.Eng. and M.Eng. (Electrical Power Devices) and a Ph.D. (Electrical Power Devices) all of the University of Nigeria in 1998, 2006 and 2014 respectively. He joined the Electrical Engineering Department, UNN as a Principal Technical Officer 2012. and was later in 2007 converted to the lecturing cadre in the same department. He is a member of Nigerian Society of Engineers (NSE). He is the current membership secretary of Nsukka Chapter of Nigerian Institute of Electrical and Electronic Engineering (NIEEE) and he is also a registered member of Council for the Regulation of Engineering in Nigeria (COREN). He has several research articles published both in local and international journals. His research areas include Machine modeling, Thermal modeling, Power and Energy systems modeling and Simulations.

